Microfluid Nanofluid (2008) 4:565–573
DOI 10.1007/s10404-007-0213-0

RESEARCH PAPER

Theoretical analysis of a new, efficient microfluidic magnetic bead separator based on magnetic structures on multiple length scales

Kristian Smistrup · Minqiang Bu · Anders Wolff · Henrik Bruus · Mikkel Fougt Hansen

Received: 7 May 2007 / Accepted: 30 July 2007 / Published online: 22 August 2007

Abstract We present a theoretical analysis of a new design for microfluidic magnetic bead separation. It combines an external array of mm-sized permanent magnets with magnetization directions alternating between up and down with μm-sized soft magnetic structures integrated in the bottom of the separation channel. The concept is studied analytically for simple representative geometries and by numerical simulation of an experimentally realistic system geometry. The array of permanent magnets provides long-range magnetic forces that attract the beads to the channel bottom, while the soft magnetic elements provide strong local retaining forces that prevent captured beads from being torn loose by the fluid drag. The addition of the soft magnetic elements increases the maximum retaining force by two orders of magnitude. The design is scalable and provides an efficient and simple solution to the capture of large amounts of magnetic beads on a microsystem platform.

Keywords Lab-on-a-chip system · High gradient magnetic separation · Magnetic beads · Bioseparation

1 Introduction

Microscopic surface-functionalized magnetic beads have been used for bioseparation in biochemical laboratories for a number of years (Safarik 1999; Safarik and Safarikova 2004). Recently, their use for bioseparation in microfluidic systems or so-called lab-on-a-chip systems has received growing interest (Verpoorte 2003; Gijs 2004; Pamme 2006).

The simplest and most prominent class of microsystems for magnetic bead separation relies on the combination of microstructures of a soft magnetic material and an externally applied magnetic field (Rida and Gijs 2004; Deng et al. 2002; Do et al. 2004; Furlani and Sahoo 2006; Furlani 2006; Smistrup et al. 2005; Lund-Olesen et al. 2007). The basic principle is that the external field magnetizes the beads and the soft magnetic structures. The latter thereby provide local magnetic field gradients that lead to the capture of the magnetic beads. This is reminiscent of the high gradient magnetic separators (HGMSs) used for large scale magnetic separation, which comprise a separation column filled with a steel wool matrix in a large external magnetic field (Watson 1973; Svoboda 2001). However, a significant difference to large scale HGMSs is that in most microsystems the magnetic material is located outside the separation channel and thus not in direct contact with the fluid sample. The magnetic forces due to microscopic magnetic structures are inherently short-ranged. One solution to overcome this limitation has been to integrate systems for magnetic separation with microfluidic mixer structures that force the beads closer to the magnetic structures resulting in substantial improvements of the capture efficiency (Lund-Olesen et al. 2007).

For some applications, magnetic beads are premixed with a dilute sample with a volume on the order of milliliter. As the separation time is limited by the diffusion of the biochemical species to the surface of the beads, a substantial number of beads has to be used to maintain a

K. Smistrup · M. Bu · A. Wolff · H. Bruus · M. F. Hansen (✉)
MIC, Department of Micro and Nanotechnology,
Technical University of Denmark, Building 345 East,
2800 Kongens Lyngby, Denmark
e-mail: mfh@mic.dtu.dk

separation time on the order of minutes. Thus, we are faced with the challenge of constructing microsystems that efficiently capture substantial amounts of beads introduced at a high volume flow rate.

In this work, we present a new "multiple length scale" solution, sketched in Fig. 1, that combines an external array of mm-sized permanent magnets outside the system with microfabricated μm-sized soft magnetic elements placed very close to the bottom of the fluid channel. The basic concept is that the permanent magnet array provides long range magnetic forces attracting the beads to the channel bottom where the soft magnetic elements are situated. The soft magnetic elements are magnetized by the permanent magnets and provide strong local forces that retain the beads at the channel bottom.

First, we illustrate that an array of permanent magnets with alternating magnetization directions provides much stronger forces attracting the beads to the channel bottom than a single large permanent magnet. We show that the optimum lateral magnet dimension is roughly twice the distance from the top face of the magnet to the channel top.

Next, we demonstrate the concept of "multiple length scale" design and its force scaling for a simplified analytical model shown in Fig. 2.

Finally, we present a detailed numerical finite element analysis of the effect for a specific geometry chosen with experimentally realistic parameters (Fig. 1). In this geometry, long permanent magnets parallel to the horizontal *z*-axis (out-of-plane in Fig. 1) are placed next to each other 0.5 mm below the bottom of the fluid channel. Their cross-section in the vertical *xy*-plane is 2×2 mm^2 (the large length scale), and their magnetization directions alternate

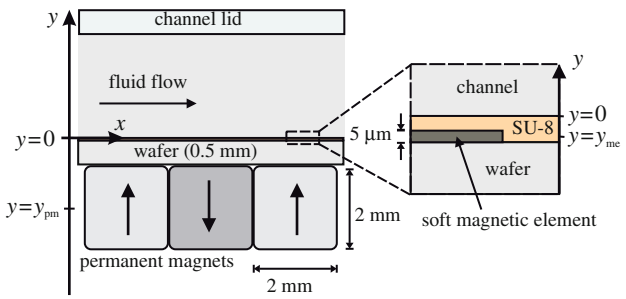

Fig. 1 Schematic illustration of the cross-section geometry of the system. Permanent magnets with alternating magnetizations are integrated in the chip holder and provide long range magnetic forces attracting magnetic beads to the channel bottom ($y = 0$). The zoom-in shows part of a soft magnetic element integrated in the chip. To create a smooth channel bottom and to separate the elements from the fluid, the elements are covered by a planarization layer (e.g., SU-8) with a thickness of 5 μm. The magnetic elements provide short range magnetic forces that aid in the bead capture and prevent beads from rolling along the channel bottom

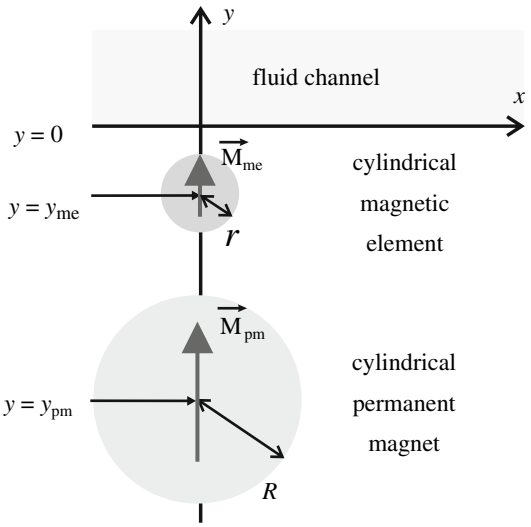

Fig. 2 Schematic of the simple analytical model with two parallel magnetic cylinders placed along the *z*-axis. The fluid channel is along the *x*-axis. The forces are calculated on the *y*-axis only. The large disk with radius R is the permanent magnet with the remanent magnetization M_{pm} in the positive *y*-direction. The smaller disk with radius r is the magnetic element with the saturated magnetization M_{me} in the positive *y*-direction

between the positive and negative *y*-direction. Soft magnetic elements with a cross-section in the vertical *xy*-plane of 200×5 μm^2 (the small length scale) are microfabricated on top of a 0.5 mm thick wafer placed on top of the permanent magnets. We label variables related to the permanent magnet and the magnetic elements with "pm" and "me", respectively. For our numerical analysis, we have chosen the soft magnetic material to have properties similar to permalloy. The soft magnetic elements are covered by 5 μm material that constitutes the planar bottom of the microchannel. The walls of the channel can then be constructed on top of the planarized channel bottom and a lid can be bonded onto the chip. The channel can have an arbitrary width in the *z*-direction. The material for the channel bottom and the channel walls could be the photodefinable epoxy resin, SU-8.

Both the simplified analytical studies and the finite element analysis show that substantial magnetic capturing and retaining forces can be obtained in a microchannel. The permanent magnet array provides a strong force attracting beads towards the channel bottom that varies only little over the height of the microfluidic channel. The soft magnetic elements enhance the retaining force acting on the beads by up to two orders of magnitude. This simple design provides the means to efficiently capture large amounts of magnetic beads in fluid channels capable of large fluid volume flows.

2 Theory

2.1 Magnetostatics and magnetic forces

We choose to write the magnetic flux density as

$$\mathbf{B} = \mu\mathbf{H} + \mu_0\mathbf{M}_0, \tag{1}$$

where μ is the field-dependent magnetic permeability, μ_0 is the permeability of free space, $\mathbf{H}$ is the magnetic field intensity and $\mathbf{M}_0$ is a permanent, field-independent magnetization. In the absence of free electrical currents, the magnetic scalar potential ϕ can be introduced, such that $\mathbf{H} = -\nabla\phi$. Further, using that $\nabla \cdot \mathbf{B} = 0$, we obtain

$$\nabla \cdot (-\mu\nabla\phi + \mu_0\mathbf{M}_0) = 0. \tag{2}$$

This is the differential equation used for determining the $\mathbf{H}$-field in the finite element analysis below.

The force on a magnetic bead is given by (Engel and Friedrichs 2002)

$$\mathbf{F} = \mu_0 \int_V (\mathbf{M} \cdot \nabla)\mathbf{H} \mathrm{d}V, \tag{3}$$

where $\mathbf{M}$ is the field-dependent bead magnetization. Note, that $\mathbf{H}$ in Eq. (3) is the magnetic field intensity in the absence of the bead. In our case the external field is so strong that the bead magnetization can be considered equal to its saturation value M_b. Assuming a small variation of the integrand over the bead, we write

$$\mathbf{F} \simeq V_\mathrm{b} M_\mathrm{b} \mathbf{G}, \tag{4}$$

where V_b is the bead volume and $\mathbf{G}$ [T/m] is the magnetic field gradient in the direction of $\mathbf{H}$ given by

$$\mathbf{G} = \mu_0(\mathbf{e}_H \cdot \nabla)\mathbf{H}, \tag{5}$$

where $\mathbf{e}_H \equiv \mathbf{H}/H$. Thus, the magnetic force on a bead equals the saturation bead magnetic moment, $V_\mathrm{b}M_\mathrm{b}$, multiplied by $\mathbf{G}$, which we will refer to as the effective magnetic field gradient. The latter is independent of the bead type, and therefore we choose it as the measure we report in the numerical section.

In the discussion it will be illustrative to relate the calculated effective magnetic field gradients to bead velocities. As a numerical example, we have chosen MyOne magnetic beads (Invitrogen, CA, USA) with diameter $d_\mathrm{b} = 1.05$ μm, which are commonly used for magnetic bioseparation. The bead saturation magnetization is $M_\mathrm{b} = 40$ kA/m (Fonnum et al. 2005) and the fluid is chosen to be water with a viscosity of $\eta = 1.0$ mPa s. Balancing the magnetic force [Eq. (4)] with the fluid drag force ($\mathbf{F}_\mathrm{d} = -3\pi\eta d_\mathrm{b}\mathbf{v}_\mathrm{b}$) yields the magnetophoretic bead velocity

$$\mathbf{v}_\mathrm{b} = \mu_\mathrm{mb}\mathbf{G}, \tag{6}$$

where μ_mb is the magnetic mobility given by

$$\mu_\mathrm{mb} \equiv \frac{M_\mathrm{b} d_\mathrm{b}^2}{18\eta} = 2.5 \times 10^{-6} \frac{\mathrm{m}^2}{\mathrm{Ts}}. \tag{7}$$

This conversion factor makes it easy to relate the calculated effective magnetic field gradients to bead velocities.

2.2 Force considerations for a single permanent magnet

First, we consider the force obtained using a single permanent magnet. For the simplicity of the arguments, we only consider the axial field from a homogeneously axially magnetized cylindrical magnet of diameter $2R$, length L and magnetization M_pm. Using a standard solenoid representation of the magnetized cylinder, this field becomes

$$H(y) = \frac{M_\mathrm{pm}}{2}\left(\frac{L + y - y_0}{\sqrt{(L + y - y_0)^2 + R^2}} - \frac{y - y_0}{\sqrt{(y - y_0)^2 + R^2}}\right). \tag{8}$$

Here, the channel bottom is placed at $y = 0$ and the top face of the permanent magnet is at $y = y_0$. To simplify the expressions and to obtain an upper limit of the magnetic force, we consider below an infinitely long cylinder ($L = \infty$). In this limit, Eq. (8) becomes

$$H(y) = \frac{M_\mathrm{pm}}{2}\left(1 - \frac{y - y_0}{\sqrt{(y - y_0)^2 + R^2}}\right). \tag{9}$$

It can easily be shown that the effective magnetic field gradient along the axis of the magnet is

$$G_y(y) = -\frac{\mu_0 M_\mathrm{pm}}{2} \frac{R^2}{\left[R^2 + (y - y_0)^2\right]^{3/2}}. \tag{10}$$

The numerically largest value of G_y is obtained at the top face of the magnet, $G_y(y_0) = -\mu_0 M_\mathrm{pm}/2R$, and G_y has dropped to half of this value when $y - y_0 = [2^{2/3} - 1]^{1/2}R \approx 0.8R$. Thus, the maximum force scales as R^{-1} and the range of the magnetic field gradient and force is about half of the lateral dimension of the magnet. Therefore, the optimum lateral dimension of the magnet is roughly twice the distance from the top face of the magnet to the top of the fluid channel.

For $y_0 = -0.5$ mm and a typical Nd-Fe-B magnet with $\mu_0 M_\mathrm{pm} = 1.2$ T and diameter $2R = 10$ mm, one finds $G_y(0) = -1.2 \times 10^2$ T/m for the infinitely long magnet and

$G_y(0) = -3.2 \times 10^1$ T/m for a 2 mm long magnet. The corresponding MyOne bead velocities obtained using Eq. (6) are –0.3 and –0.08 mm/s, respectively. For a smaller magnet with the more optimal lateral dimension $2R = 2$ mm, this value increases to $G_y(0) \simeq -4.3 \times 10^2$ T/m (infinitely long magnet) and $G_y(0) \simeq -4.0 \times 10^2$ T/m (2 mm long magnet), respectively. Hence, for a magnet with a realistic thickness the force attracting the beads to the channel bottom can be enhanced by an order of magnitude by going from a cm-sized magnet to an optimized mm-sized magnet.

These arguments clearly show the advantage of using smaller magnets. Note, that if several magnets are arranged with the magnetization directions in the same direction they correspond to a single larger magnet. An array of magnets with alternating magnetization directions with dimensions comparable to half the distance to the top of the microfluidic channel will ensure that the magnetic field and the magnetic field gradient are localized and concentrated in the channel.

2.3 Scaling of forces in a simple analytical model

To illustrate the basic principle of further enhancing the magnetic forces by including soft magnetic elements at the bottom of the channel and the scaling of the forces, we calculate the magnetic forces on a bead due to a permanent magnet and a magnetic element separately for the simple 2D two-body model sketched in Fig. 2. Both the permanent magnet and the magnetic element are shaped as infinitely long cylinders parallel to the z-axis (out-of-plane). The channel bottom is at $y = 0$ and the centers of the permanent magnet and soft magnetic element are placed at $y = y_{\mathrm{pm}}$ and $y = y_{\mathrm{me}}$, respectively. For simplicity we consider only the magnetic field intensity on the y-axis. With this choice of geometry, the magnetic field and the magnetic field gradient are parallel to the y-axis and we write $\mathbf{H} = H(y)\mathbf{e}_y$. We assume that both the permanent magnet and the magnetic element are homogeneously magnetized with magnetizations M_{pm} and M_{me}, respectively, and that the magnetic element is magnetically saturated. In this case, the 2D dipole fields H_{pm} and H_{me} from the permanent magnet and the magnetic element on the y-axis can be obtained by solving Laplace's equation for the magnetic scalar potential in cylindrical coordinates [see, e.g., (Watson 1973)] and are

$$H_{\mathrm{pm}}(y) = \alpha_1 \frac{R^2 M_{\mathrm{pm}}}{(y - y_{\mathrm{pm}})^2}, \tag{11}$$

$$H_{\mathrm{me}}(y) = \alpha_1 \frac{r^2 M_{\mathrm{me}}}{(y - y_{\mathrm{me}})^2}, \tag{12}$$

where the radii r and R are defined in Fig. 2 and α_1 is a constant. The magnetic forces on a bead due to the permanent magnet and the magnetic element are obtained from Eqs. (4) and (5) as

$$F_{\mathrm{pm}}(y) = \alpha_2 \frac{R^2 M_{\mathrm{pm}}}{(y - y_{\mathrm{pm}})^3}, \tag{13}$$

$$F_{\mathrm{me}}(y) = \alpha_2 \frac{r^2 M_{\mathrm{me}}}{(y - y_{\mathrm{me}})^3}, \tag{14}$$

where α_2 is a new constant. Thus, the ratio of the two forces becomes

$$\frac{F_{\mathrm{me}}(y)}{F_{\mathrm{pm}}(y)} = \left(\frac{r}{R}\right)^2 \left(\frac{M_{\mathrm{me}}}{M_{\mathrm{pm}}}\right) \left(\frac{y - y_{\mathrm{pm}}}{y - y_{\mathrm{me}}}\right)^3. \tag{15}$$

Typical parameters for microsystems are $r \simeq 5$ μm and $R \simeq 1$ mm, yielding $r/R \simeq 5 \times 10^{-3}$, and $M_{\mathrm{me}} \simeq M_{\mathrm{pm}}$. If the permanent magnet is placed on the back side of a 0.5 mm thick wafer on which the magnetic element and the fluid channel are fabricated on the front side, typical values are $y_{\mathrm{pm}} \simeq -1.5$ mm and $y_{\mathrm{me}} \simeq -10$ μm, i.e., $y_{\mathrm{me}}/y_{\mathrm{pm}} \simeq 7 \times 10^{-3}$. At the channel bottom, $y = 0$, these parameters yield the ratio of forces

$$\frac{F_{\mathrm{me}}(0)}{F_{\mathrm{pm}}(0)} \simeq 84. \tag{16}$$

Moreover, it is found that $F_{\mathrm{me}}(y)/F_{\mathrm{pm}}(y) \simeq 1$ when $y \simeq 35$ μm. Thus, the element strongly enhances the magnetic force on the beads in the vicinity of the magnetic element.

3 Finite element analysis

In this section, we calculate the magnetic force on beads in a microchannel for the realistic geometry of Fig. 1. This geometry can be represented by the model geometry reduced by symmetry arguments, which is illustrated in Fig. 3a that we solve numerically using the finite element method. We investigate the sensitivity of our calculations of the magnetic force to the gap $2g_{\mathrm{pm}}$ between the permanent magnets in the permanent magnet array and the radius of curvature ρ_{pm} of the edges of the permanent magnets as these parameters are important for the convergence and accuracy of the calculations.

In Sect. 4, we calculate the effect of adding the soft magnetic elements at different positions relative to the permanent magnet.

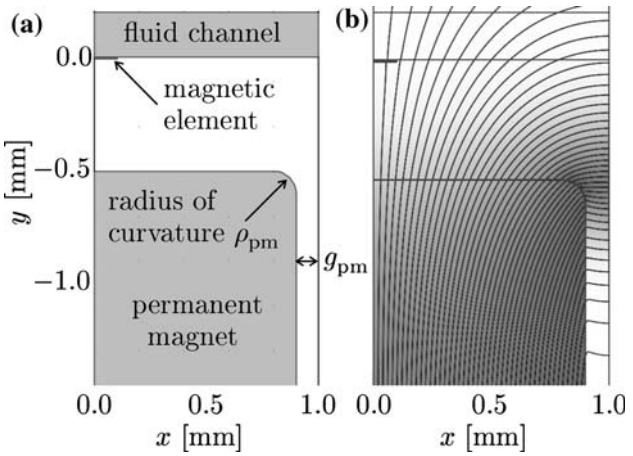

Fig. 3 **a** Zoom-in of the model geometry. The figure shows half of one of the permanent magnets, the position of the fluid channel, and the position of a soft magnetic element. The magnetic element has a height of 5 μm, a total width of 200 μm and is placed with its top 5 μm below the bottom of the channel. The total calculation domain extends from y = –100 to 100 mm. The solution ϕ is symmetric and antisymmetric around the vertical boundaries at x = 0 and 1 mm, respectively. The gap $2g_{pm}$ between adjacent permanent magnets and the radius of curvature ρ_{pm} of the permanent magnet edges are defined. **b** Example of calculated field lines for the magnetic flux density. Near the corner of the magnet, the flux density attains its maximum value of about 1.3 T. In the fluid channel it attains values in the range 0.2–0.4 T with the lowest value at the top of the channel

Prior to the numerical investigations of the specific geometry below, the finite element analysis was validated against known analytical results for a simple geometry.

3.1 Geometry and boundary conditions

Figure 3a shows the geometry and calculation domain of our model. The boundary conditions used in conjunction with Eq. (2) are implemented in Comsol Multiphysics 3.3 as

$$\hat{\mathrm{n}} \cdot \nabla\phi = 0, \quad x = 0\,\mathrm{mm}, \tag{17}$$

$$\phi = 0, \quad x = 1\,\mathrm{mm}, \tag{18}$$

$$\hat{\mathrm{n}} \cdot \nabla\phi = 0, \quad y = 100\,\mathrm{mm}, \tag{19}$$

$$\hat{\mathrm{n}} \cdot \nabla\phi = 0, \quad y = -100\,\mathrm{mm}, \tag{20}$$

where $\hat{\mathrm{n}}$ denotes the outward normal vector of the boundary.

Conditions (17), (19) and (20) cause field lines to be parallel to the corresponding boundaries, while condition (18) causes the field lines to be perpendicular to the x = 1 mm boundary. These conditions correspond to H_x being antisymmetric around x = 0 mm and symmetric around x = 1 mm, while H_y is symmetric around x = 0 mm and antisymmetric around x = 1 mm. Likewise, G_x is antisymmetric around both x = 0 and 1 mm, whereas G_y is symmetric around both x = 0 and 1 mm.

Hence, the simulation domain corresponds to half the width of one permanent magnet in an infinite 1D array of permanent magnets along the x-axis with magnetization directions alternating between the positive and negative y-direction as sketched in Fig. 1.

The magnetization of the permanent magnet was set to the constant value $\mathbf{M}_0 = M_{pm}\mathbf{e}_y$. We chose $\mu_0 M_{pm}$ = 1.2 T, which is a typical value for Nd-Fe-B magnets. The permeability of the soft magnetic material was set to

$$\mu = \mu_0\left[1 + \frac{M_{me}}{H}\tanh\left(\frac{\chi_0 H}{M_{me}}\right)\right], \tag{21}$$

with χ_0 = 1,000 and $\mu_0 M_{me}$ = 1.25 T to emulate the magnetization curve of permalloy. This expression for the permeability shows the correct behavior in the limits $H \to 0$ and $H \to \pm\infty$ and is one of several possible choices for approximating the magnetization curve of a soft magnetic material. The magnetization behavior is largely dominated by demagnetization effects and is thus insensitive to the detailed shape of the intrinsic magnetization curve of the soft magnetic material.

In the model shown in Fig. 3a, we have introduced both the gap g_{pm} from the edge of the permanent magnet to the symmetry axis at x = 1 mm and the curvature of radius ρ_{pm} of the edge of the magnet. These features will always be present in a real system. Moreover, the introduction of the gap and curvature substantially improves convergence of the calculations and reduces the numerical uncertainty. This is due to the fact that the magnetic potential diverges near the corners of two adjacent permanent magnets with opposite magnetization placed next to each other and that the finite element solver does not handle divergences well. Introduction of a curvature of the corner also reduces the need for mesh resolution near the corner. The effects of different gaps and radii of curvature of the edges of the permanent magnets are investigated in Sect. 3.2.

3.2 Investigation of magnet gap and edge curvature

Figure 3b shows an example of magnetic flux density field lines calculated for the geometry in Fig. 3a by solving Eq. (2) with boundary conditions (17)–(20). The calculation was carried out in Comsol Multiphysics 3.3 using third order elements. The standard mesh was set up as "Normal mesh" except that the "Element growth rate" was set to 1.2, and "Resolution of narrow regions" was set to 3, and the "Maximum element size" was set to 10 μm in the fluid channel subdomain, where we wish to measure **G**.

We aim to find values of g_{pm} and ρ_{pm} for the permanent magnet edge that allow for a maximum deviation of G of 1% in the microchannel relative to a reference geometry. We cannot use an analytic solution as reference geometry, since no such solution exists. Therefore, we use as reference the geometry that has the smallest possible gap and/or the smallest possible radius of curvature. The geometries used for reference are defined in the caption of Fig. 4. Figure 4 shows the results of this investigation. Each magnet had a fixed height of 2 mm and a total width of $2 \times (1\text{ mm} - g_{pm})$. Note that the reference values of the magnet gap g_{pm} and the radius of curvature ρ_{pm} of the edge of the permanent magnet are both much smaller than the distance between the permanent magnets and to the fluid channel. In Fig. 4 we estimate the numerical error in our calculations. The mesh was refined once more than the mesh used for calculations, and the graph shows the normalized magnitude of the change in the result as a function of position. It is observed that a deviation in the calculation of **G** smaller than 1% relative to the refined mesh can be obtained with the standard mesh, $g_{pm} = 0.03$ mm and $\rho_{pm} = 0.1$ mm. This deviation was measured 20 μm above the channel bottom. We will also be reporting **G** at the channel bottom, so for completeness, we report that the maximum change in **G** due to refining the mesh is approximately 10% at the channel bottom (data not shown). As we shall see, the effect we are investigating gives order-of-magnitude changes, so an error of 10% or less is negligible in this context.

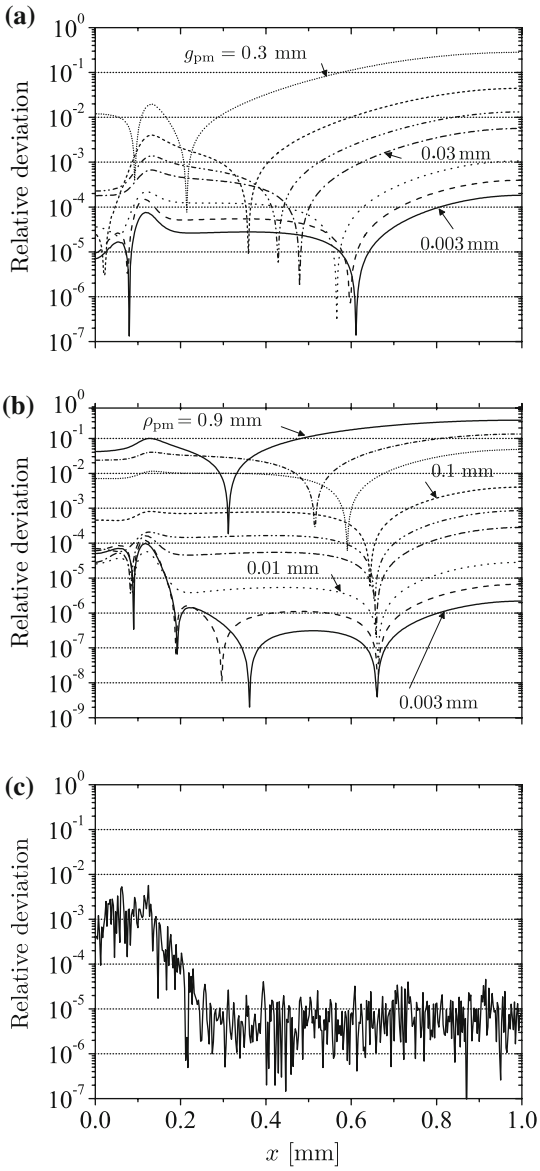

Fig. 4 Results of the numerical investigation of the magnet gap and edge curvature of the permanent magnet. All results were calculated at $y = 20$ μm. **a** Relative deviation, $|G_y(g_{pm})/G_y(g_{pm}^{(0)})-1|$ with $g_{pm}^{(0)} = 0.001$ mm, calculated for the magnet gaps $g_{pm} = 0.3, 0.1, 0.05, 0.03, 0.01, 0.005, 0.003$ mm and a radius of curvature of $\rho_{pm} = 0.1$ mm. **b** Relative deviation, $|G_y(\rho_{pm})/G_y(\rho_{pm}^{(0)})-1|$ with $\rho_{pm}^{(0)} = 0.001$ mm, calculated for the radii $\rho_{pm} = 0.9, 0.5, 0.3, 0.1, 0.05, 0.03, 0.01, 0.005, 0.003$ mm and a gap of $g_{pm} = 0.03$ mm. **c** Relative change in G_y when the standard mesh is refined one time. The calculation was performed for a gap of $g_{pm} = 0.03$ mm and a radius of curvature of $\rho_{pm} = 0.1$ mm

4 Results and discussion

We have performed a finite element analysis of the infinite array of permanent magnets with magnetization directions alternating between the positive and negative y-direction represented by the calculation geometry in Fig. 3a. The permanent magnet array was set up as described in Sect. 3 with $\rho_{pm} = 0.1$ mm and $g_{pm} = 0.03$ mm. Thus, a permanent magnet is placed in the simulation domain with its horizontal center at $x = 0$ mm and its edge at $x = 0.97$ mm, i.e., $x = 1$ mm corresponds to the middle of the gap between adjacent permanent magnets with opposite magnetization orientations. Figure 5 shows the variation of G_y and G_x calculated at the indicated distances above the channel bottom without soft magnetic elements and with soft magnetic elements at the indicated positions.

4.1 Magnetic force without soft magnetic elements

We first discuss the results when no soft magnetic elements are present. For this case, the effective magnetic field gradient can be seen as the thick, dashed lines in Fig. 5. The effective magnetic field gradient in the y-direction, Fig. 5a, attains values that are essentially independent of the height above the channel bottom as all studied y-values are small compared to the dimensions of a magnet. The values of G_y are symmetric around $x = 0$ and negative for all x. The values are numerically largest ($G_y \simeq -$

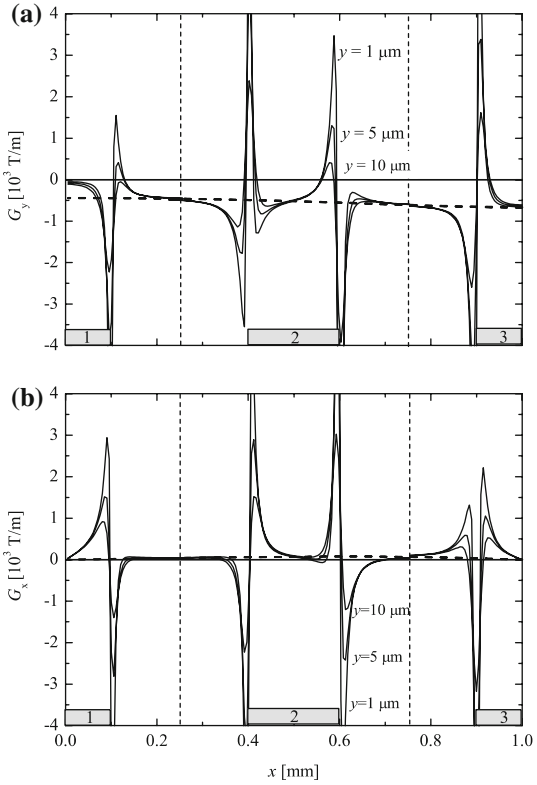

Fig. 5 Results of the numerical calculation for the geometry in Fig. 3a representing an infinite array of magnets. An upwards magnetized permanent magnet with g_{pm} = 0.03 mm and ρ_{pm} = 0.1 mm is placed in the simulation domain with its center at (x,y) = (0 mm,–1.51 mm). **a** and **b** show G_y and G_x, respectively, at the distances y = 1, 5 and 10 μm above the channel bottom calculated without magnetic elements (*dashed lines*) and with magnetic elements (*full lines*). The calculations with magnetic elements were carried out separately for three different element positions indicated by the *grey bars* at the x-axes. The magnetic elements are 5 μm thick, 200 μm wide (in total) and placed with their top 5 μm below the channel bottom

6.5×10^2 T/m) near the corner of a magnet ($x \simeq 1$ mm). Above the center of a magnet (x = 0 mm), the value of G_y reduces slightly to $G_y \simeq -4.5 \times 10^2$ T/m. Using Eq. (6), these numbers correspond to MyOne magnetophoretic bead velocities of –1.6 and –1.1 mm/s, respectively. Note that the values correspond well to that resulting from the simplified analytical treatment in Sect. 2.2.

The values of G_x due to the permanent magnets are positive for the x-values shown in Fig. 5b, but attain much smaller numerical values (not discernible in the figure) ranging from the maximum value $G_x \simeq 0.8 \times 10^2$ T/m ($v_b \simeq 0.2$ mm/s) near $x \simeq 0.6$ mm to 0 T/m for x = 0 and 1 mm. G_x is antisymmetric around x = 0 mm and therefore attains negative values for $-1 < x < 0$ mm.

Thus, the permanent magnet array provides a strong force attracting the beads towards the bottom of the channel. However, the force in the x-direction is weak in comparison and attracts the beads towards the gap between the permanent magnets. Due to the weak forces in the x-direction, the beads may tend to be torn loose by the fluid drag and roll along the channel bottom when a fluid flow is applied.

4.2 Magnetic force with soft magnetic elements

We now discuss the effect of the presence of soft magnetic elements. The solid lines in Fig. 5 show the effect of elements placed at the three different positions indicated by the grey boxes labeled 1–3 at the x-axes. Separate calculations were carried out for each of the studied element positions. It is seen that the contribution to **G** from an element decreases rapidly with the distance from the element in the x-direction and is negligible outside the dashed vertical lines in the figure. We have therefore chosen to plot each contribution only between the indicated vertical dashed lines.

From Fig. 5a, it is seen that the effect of the elements on G_y is to superpose a number of spikes near the corners of the magnetic elements on top of the slowly varying contribution from the permanent magnet. The magnitude of the spikes in G_y is highest near $x \simeq 0.5$ mm and attains numerical values up to 1.5×10^4 T/m at y = 1 μm. Note, that G_y is symmetric around both x = 0 and 1 mm. Beads close to the channel bottom will be strongly attracted to the channel bottom near the negative spikes and repulsed from channel bottom near the positions where the positive spikes lead to $G_y > 0$. The effect of the soft magnetic elements on the capture of beads further up in the channel is less clear. An inspection of the areas of the positive and negative peaks due to the magnetic elements using the symmetry of G_y yields that the average effect of elements on the force in the y-direction is negligible. Thus, as the beads are traveling in the upper region of the channel, the effect of the soft magnetic elements is to perturb the bead trajectories up and down around the "average" trajectory due to the permanent magnets. When the "average" position of the beads gets below a certain height, the beads are rapidly pulled to the bottom of the channel and kept there by the soft magnetic elements.

In the x-direction, the elements lead to spikes in G_x with magnitudes up to 1.5×10^4 T/m at y = 1 μm. The force in the x-direction attracts beads to regions, where a positive spike is followed by a negative spike (e.g., x = 0.6 mm), and repulses them from regions, where a negative spike is followed by a positive spike (e.g., x = 0.4 mm). The maximum values of G_x keeping the beads fixed at the attractive regions now have a magnitude with the magnetic elements in the range $0.2–1.5 \times 10^4$ T/m compared to less than 0.8×10^2 T/m without the magnetic elements. The

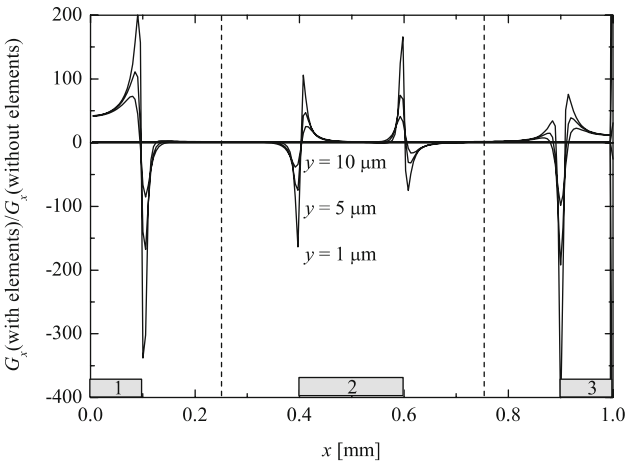

Fig. 6 Values of G_x calculated with soft magnetic elements relative to those calculated without soft magnetic elements at the distances y = 1, 5 and 10 μm above the channel bottom

corresponding maximum MyOne bead magnetophoretic velocities with and without magnetic elements are 5–37 and 0.2 mm/s, respectively. Thus, the relative effect of the magnetic elements is much more pronounced in the x-direction.

Figure 6 shows the values of G_x calculated with soft magnetic elements relative to those calculated without soft magnetic elements. It is seen that G_x increases with a factor of up to 400 due to the soft magnetic elements depending on the position of the element. This 100-fold increase implies that assemblies of captured magnetic beads are much more robust against being torn loose or rolling along the channel bottom with the fluid flow in the channel.

5 Conclusions

We have theoretically and numerically investigated a new design of a magnetic bead separator combining mm-sized permanent magnets with μm-sized soft magnetic elements by analytical calculations for simplified models and a finite element analysis for a realistic microsystem geometry. The two analyses yield effects on the same order of magnitude.

The permanent magnet array provides significant magnetic forces, extending over a length scale of about half the lateral magnet dimension, that effectively attract the magnetic beads to the bottom of the channel. This force exceeds that from a single larger permanent magnet by an order of magnitude. The magnetic force retaining the beads at the channel bottom due to the permanent magnet array, however, is comparatively weak leaving the beads susceptible to being torn loose or to rolling when a fluid is flowing in the channel. The soft magnetic elements, integrated with the microchannel and magnetized by the field from the permanent magnets, however, provide a further increase of the maximum retaining force on the magnetic beads by two orders of magnitude. These very strong local magnetic forces substantially reduce the effect of a fluid flow on the stability of the bead assemblies and facilitate the robust capture of more magnetic beads at a given fluid flow rate.

The permanent magnets can be integrated into the chip holder and the soft magnetic elements are relatively simple to integrate in fabrication schemes. The advantage of the "multiple length scale" design over designs incorporating magnetic structures under or adjacent to the microchannel in a homogeneous applied field (Furlani and Sahoo 2006; Furlani 2006; Smistrup et al. 2005; Lund-Olesen et al. 2007) is the long range (tuned to the distance to the top of the microfluidic channel) and the significantly higher strength of the capturing forces along the channel height. Compared to designs with magnetic structures adjacent to the microchannel (Smistrup et al. 2005; Lund-Olesen et al. 2007), a potential further advantage is the scalability of the channel width and the capacity for capturing large amounts of beads. Thus, the present design can be utilized for applications where a large number of magnetic beads is to be separated from a fluid at a high flow rate.

Acknowledgments K. Smistrup acknowledges support from Copenhagen School of Nanotechnology (C:O:N:T) and the Danish Technological Institute. M. Bu acknowledges support from EU FP6 STREP project OPTOLABCARD (contract no 016727).

References

Safarik I (1999) Use of magnetic techniques for the isolation of cells. J Chromatogr B: Biomed Sci Appl 722(1–2):33–53

Safarik I, Safarikova M (2004) Magnetic techniques for the isolation and purification of proteins and peptides. Biomagn Res Technol 2:7

Verpoorte E (2003) Beads and chips: new recipes for analysis. Lab Chip 3:60N–68N

Gijs MAM (2004) Magnetic bead handling on-chip: new opportunities for analytical applications. Microfluid Nanofluid 1:22–40

Pamme N (2006) Magnetism and microfluidics. Lab Chip 6:24–38

Rida A, Gijs MAM (2004) Manipulation of self-assembled structures of magnetic beads for microfluidic mixing and assaying. Anal Chem 76(21):6239–6246

Deng T, Prentiss M, Whitesides GM (2002) Manipulation of magnetic microbeads in suspension using micromagnetic systems fabricated with soft lithography. Appl Phys Lett 80:461–463

Do J, Choi J-W, Ahn CH (2004) Low-Cost magnetic interdigitated array on a plastic wafer. IEEE Trans Magn 40:3009–3011

Furlani EP, Sahoo Y (2006) Analytical model for the magnetic field and force in a magnetophoretic microsystem. J Phys D: Appl Phys 39(9):1724–1732

Furlani EP (2006) Analysis of particle transport in a magnetophoretic microsystem. J Appl Phys 99(2):024912

Smistrup K, Kjeldsen BG, Reimers JL, Dufva M, Petersen J, Hansen MF (2005) On-chip magnetic bead microarray using

hydrodynamic focusing in a passive magnetic separator. Lab Chip 5(11):1315–1319

Lund-Olesen T, Bruus H, Hansen MF (2007) Quantitative Characterization of Magnetic Separators: Comparison of Systems with and without Integrated Microfluidic Mixers. Biomed Microdevices 9:195–205

Watson JHP (1973) Magnetic filtration. J Appl Phys 44(9):4209–4213

Svoboda J (2001) A realistic description of the process of high-gradient magnetic separation. Miner Eng 14(11):1493–1503

Engel A, Friedrichs R (2002) On the electromagnetic force on a polarizable body. Am J Phys 70:428

Fonnum G, Johansson C, Molteberg A, Mørup S, Aksnes E (2005) Characterization of Dynabeads by magnetization measurements and Mössbauer spectroscopy. J Magn Magn Mat 293:41–47